Dynamic delay-dispersive UWB-Radar Targets: Modeling and Estimation

Jonas Gedschold*, Sebastian Semper*, Reiner S. Thomä*, Michael Döbereiner†, Giovanni Del Galdo*,†

***Abstract*—This publication proposes a parametric data model and a gradient-based maximum likelihood estimator suitable for the description of delay-dispersive responses of multiple dynamic UWB-radar targets. The target responses are estimated jointly with the global target parameters range and velocity. The large relative bandwidth of UWB has consequences for model-based parameter estimation. On the one hand, the Doppler effect leads to a dispersive response in the Doppler spectrum and to a coupling of the target parameters which both need to be considered during modeling and estimation. On the other hand, the shape of an extended target results in a dispersive response in range which can be resolved by the radar resolution. We consider this extended response as a parameter of interest, e.g., for the purpose of target recognition. Hence, we propose an efficient description and estimation of it by an FIR structure only imposing a restriction on the target's dispersiveness in range. We evaluate the approach on simulations, compare it to state of the art solutions and provide a validation on measurement data.**

***Index Terms*—Ultra-Wideband Radar, Extended Target Model, Velocity Model, Doppler effect, High-resolution Parameter Estimation**

I. Introduction

THE range resolution of a radar system essentially depends on the bandwidth. A wide bandwidth is readily available at millimeter and sub-THz frequencies. Given a large bandwidth, the shape of an extended target shows up as a characteristic signature that is resolved in fast time (or range). However, some radar applications additionally require lower frequencies for manifold reasons. One advantage is the ability to penetrate materials, which improves with lower frequencies. Well-known applications include ground penetrating radar or through-wall radar [1]–[4]. Other reasons that require specific (and often lower) frequencies relate to the detection of characteristic molecular or structural resonances [5].

The frequency band of interest can range from a few hundred MHz to several GHz where the latter is often termed Ultra-Wideband (UWB). In this paper, we assume a large relative bandwidth [2], [6] resulting from a large absolute bandwidth of several GHz at low frequencies. For example, a relative bandwidth of more than 20% of the carrier frequency can be considered decisive for UWB.

Large relative bandwidths may cause issues with circuit design and algorithms. Considering signal parameter estimation, several algorithms are built on *narrowband assumptions*, i.e., model simplifications which are only valid for small relative bandwidths. A prominent example is the derivation of the velocity from the Doppler shift. Even with a wide bandwidth one can still apply this principle of velocity estimation. However, this approach needs to be revised when the fractional bandwidth increases, as it is the case with UWB [7], [8]. Another example of invalid narrowband assumptions is, that the target parameters range and velocity cannot be estimated separately anymore. Both effects are detailed in the sequel. In general, parameter estimation using wrong model assumptions becomes inherently biased since there is a mismatch between the model and the measured data [9], [10].

In traditional radar signal processing the range-Doppler map, also known as scattering function [11]–[13], is estimated by a 2D Fast Fourier Transform (FFT) assuming periodically repeated transmit signals. Typical examples are multicarrier sequences (OFDM) or maximum length binary sequences (MLBS). A matched filter response in the frequency domain transforms to fast time where the short correlation function indicates the target range. The respective Fourier transform along slow time yields the Doppler domain and the relative target speed is attributed to a *Doppler shift* resolved in delay and Doppler. However, from a physical point of view, the Doppler effect is a temporal scaling that can only be approximated as a frequency shift if the relative bandwidth of the waveform is small. Strictly speaking, the Doppler effect only results in a frequency shift for a sine wave.

Given UWB waveforms, a constant relative speed does not appear as a peak in the Doppler spectrum limited to a single range-Doppler resolution bin. It rather results in a dispersive response such that a Doppler shift-based model is not suitable for speed estimation. Hence, a modified formulation of the data model is required that includes the relative velocity as an explicit parameter. A further issue arises from the range migration of the impulse when the target is moving relative to the sensor. If the coherent integration time is chosen long enough (to increase the Doppler resolution) the pulse position migrates to the next range-Doppler resolution bin. Thus, the Doppler and range dimensions are no longer independent [14]. Finally, the Doppler effect additionally affects the observed characteristic signature of an extended target due to a time-scaling of its response. If we want to model and evaluate this response we need to know, on the one hand, the scaled waveform at the moment it hits the target. On the other hand, the target response to the scaled waveform is affected again by the Doppler effect on the way to the receiver. At the receiver, only the combined Doppler influence on the transmitting and receiving path is observable which needs to be considered

* Institute for Information Technology, TU Ilmenau, Helmholtzplatz 2, 98693 Ilmenau, Germany, † Fraunhofer Institute for Integrated Circuits (IIS), Am Vogelherd 90, Ilmenau, Germany

Acknowledgments: This work is partly funded by the DFG projects SeMoCa with project number 420546347 and HoPaDyn with Grant-No. TH 494/30-1.

during target response estimation.

When it comes to modeling the characteristics of extended targets, current algorithms only allow this to a limited extent. Common multipath estimators (such as RIMAX [15]) assume a point-like interaction. Since an extended target spans a range of multiple resolution cells it could be described by several reflection points. However, describing extended targets in this way would require an estimation of multiple and independent global range-velocity parameter pairs. Afterwards, reflection points belonging to a single target have to be combined to a cluster of such pairs [16]. However, this approach has a drawback for the estimator. If the reflection points are closely spaced in the parameter domains, the estimated parameters are strongly correlated resulting in high parameter variances for the individual reflection points. Alternatively, the model has to be adapted to directly incorporate extended target responses. Hence, we assume that a number of adjacent range samples (with the same velocity) belong to the same target. Furthermore, we assume that the response behaves linear and time-invariant (LTI) within the observation time. Consequently, we can select an Finite Impulse Response (FIR) or Infinite Impulse Response (IIR) approach as a structural (parametric) model of the target. If the extended target response is predominantly generated by independent scattering from the target's structure without internal multipath interaction, it can be modeled as an FIR structure. If the target's response is more strongly characterized by mutual interactions of scattering centers and resonances in cavities, IIR models may be more suitable.

Modeling the delay dispersion by such a compact, target-related model relaxes the overall estimation effort, since one target is described by one global range-velocity parameter pair. Nevertheless, small variances in the target's trajectory and orientation will lead to a scintillation of the observed response resulting from reflections at structures larger than one wavelength. For point-like targets, this results in a fluctuation of amplitude and phase, requiring stochastic target descriptions such as Swerling models. Integration over time reduces the fluctuation and increases the probability of detection [17]. The response of an extended target will also be subject to a stochastic fluctuation due to the scintillation of individual scattering centers. Also in this case, the fluctuations can be reduced by observing the target response over the coherent integration time. Furthermore, large-scale changes in distances and orientation of the target can result in entirely different target responses. Hence, a physical interpretation of the model, e.g., for target recognition requires the identification of pose-invariant features or matching to known angular-resolved target responses [18], [19].

In this paper, we address two important topics: (1) relative target velocity estimation and (2) target response identification and modeling.

A. State of the Art

Many UWB radar applications have in common that either the sensing system or the radar targets are moving. An example for dynamic sensing systems is given in [20] where mobile and deployable sensing nodes cooperate in emergency situations, e.g., for environmental mapping and localization. Authors in [21], [22] focus on dynamic targets, specifically on the detection and tracking of humans. Besides a variety of dynamic scenarios, some UWB applications do not only require a detection but also a target recognition [4], [20]. The contributions in [18], [19] show, that the extended target response in a high-resolution range profile is valuable for target classification. However, extended target responses require new concepts for global target parameters as investigated in [23], e.g., for the global range of a human. To compensate Doppler spread and range migration in target velocity estimation, [8] and [14] use matched filter and Keystone transformations for range-velocity map estimation. Nevertheless, a joint estimation of the global target parameters range and velocity as well as extended target responses is not yet analyzed.

Model-based target parameter estimation is investigated in a variety of contributions aiming at radio environments. Corresponding algorithms are RIMAX [15], [24] or the approaches presented in [25]–[28]. Although these algorithms provide a comprehensive description of the wave propagation by considering, e.g., angles of departure or arrival or bistatic antenna configurations, their applicability to UWB is limited by their narrowband assumptions. Relaxing these assumptions has as consequence that the target parameters cannot be estimated separately anymore since they are coupled, e.g., by the Doppler effect. Hence, authors in [7] introduce coupling terms between range, velocity, and direction of arrival for their UWB target parameter estimator.

The aforementioned parameter estimators assume point-like targets. Hence, the underlying models do not account for any target-related spreads in the parameter domains like range. Extended targets are therefore resolved into contributions of individual scattering centers. Building on these results, clustering algorithms are used to combine the contributions into clusters [29]–[32]. Hence, a spread or dispersiveness in range is represented by a group of individual estimated scattering centers. However, prior estimation of individual scattering points can be a challenge for the estimator if the reflection points are closely spaced and, hence, differ very little in their parameters. Besides from model-based parameter estimation, authors in [33] investigate clustering algorithms on the radar detector's output to group extended target responses in the range-Doppler map.

Various mechanisms lead to a delay-dispersion of a target's response. Some physical scattering events depend on frequency such as edge or corner diffraction. These mechanisms can be physically modeled by the Geometrical Theory of Diffraction (GTD) [34]–[37]. However, considering target parameter estimation in dynamic scenarios, this would require a comprehensive electromagnetic and angular resolved model which does not generalize to different types of targets. Therefore, this approach is more suited for simulation studies.

If the target response is characterized by multipath reflections between scattering centers or strong resonant structures it can be modeled as a superposition of damped exponential functions as in [38]–[41]. Here, the resonant structures are characterized by a resonance frequency and a damping factor describing the decay over time. Similar, authors in [42] use

an exponentially decaying pulse in time domain to account for resonant structures. Assuming that both, individual scattering centers and resonant structures, contribute to the target response, the authors in [19], [43] use autoregressive and moving average (ARMA) models known from time series analysis to model extended targets. This concept is similar to composing a target response of FIR (moving average) or IIR (autoregressive) structures. However, these approaches do not consider multi-target scenarios or global target parameters.

Delay-dispersive phenomena are also known to wideband radio channel modeling and estimation. A prevalent approach is to assign each propagation path an individual frequency Transfer Function (TF) which accounts for the dispersive properties of the path. Authors in [6] propose to decompose the full TF into a number of subbands such that narrowband model simplifications are valid for each individual subband. This reduces the amount of necessary model parameters. The authors in [44] use a Space-Alternating Generalized Expectation-Maximization (SAGE) algorithm to estimate individual parameters for each subband from channel measurements. In [45] a variant of the RIMAX algorithm is applied to a subband model, although parameters like time and direction of arrival are kept constant over all bands. The advantage of these models is that they can capture a wide range of physical processes due to the generalized description of the TF. However, the approximations may hold for a narrow subband but still introduce discontinuities in the transition from one band to another which are physically hard to justify.

B. Contributions

Building on the state of the art, we propose a multi-target signal model (Section II) and a corresponding maximum likelihood (ML) parameter estimator (Section III) allowing a joint estimation of global target parameters (range and velocity) as well as the characteristic signature of a target. We model the delay-dispersive target responses as an FIR structure. This parametric representation also allows a straightforward postprocessing of the target's response. Furthermore, we perform a comprehensive analysis of the approach by simulations (Section IV), comparisons to state of the art solutions (Section IV-B2, Section IV-B3, Section IV-C1) and a measurement example (Section V).

The proposed ML estimator is based on the RIMAX algorithm [15] and allows a grid-free estimation of the global target parameters. We discuss two major extensions to the RIMAX algorithm. First, a relaxation of the Kronecker-model assumptions is required since frequency and time are coupled by the Doppler effect. Second, the delay-dispersive model for each detected target needs to be estimated by a least-squares approach. Furthermore, the estimator includes heuristics based on statistical tests for an estimation of the number of present targets.

C. Notation

Let $\boldsymbol{J}_{\boldsymbol{x}}\boldsymbol{f}$ denote the Jacobian matrix of a function $\boldsymbol{f}: \mathbb{R}^n \to \mathbb{R}^m$, which can also be a partial derivative, if $\boldsymbol{f}$ has more parameters than $\boldsymbol{x}$. Let $\boldsymbol{J}^2\boldsymbol{f}$ denote the Hessian, i,e, the second order derivatives, of the function $\boldsymbol{f}$. We denote the Frobenius norm of a matrix $\boldsymbol{A}$ via $\|\boldsymbol{A}\|_F$. Let $\mathbf{1} \in \mathbb{R}^n$ denote a vector of all ones, $\boldsymbol{A}^H$ the Hermitian transpose of the matrix $\boldsymbol{A}$, $\mathcal{O}$ the standard big-O notation and $\overline{z} \in \mathbb{C}$ the complex conjugate of $z \in \mathbb{C}$. Let $\boldsymbol{E}$ denote the expectation operator.

II. Dispersive Multi-Target Signal Model

We start with an observation Y of the time-variant transfer function S modeled by

$$Y(f,t) = S(f,t) + N(f,t)\,, \tag{II.1}$$

where N accounts for a yet to be specified additive measurement noise process. The transfer function itself is modeled as a superposition of P target responses S_p

$$S(f,t) = \sum_{p=1}^{P} S_p(f,t)\,. \tag{II.2}$$

We formulate the model for a single target response in complex baseband and time as

$$\begin{aligned} S_p(f,t) = \gamma_p(f) \cdot \exp(-\jmath \cdot 2\pi \cdot f \cdot \tau_p) \\ \cdot \exp\left(\jmath \cdot 2\pi \cdot \hat{\alpha}(f, \Delta v_p) \cdot t\right)\,, \end{aligned} \tag{II.3}$$

where $\gamma_p \colon \mathbb{R} \to \mathbb{C}$ describes the target's signature in frequency domain delayed by τ_p, Δv_p the target's velocity relative to the radar, and $\hat{\alpha} \colon \mathbb{R} \times \mathbb{R} \to \mathbb{R}$ the velocity model accounting for the coupling between frequency and time, i.e., the Doppler effect. It is worth noting that this model separates the description of the target's Transfer Function (TF) via γ and τ from the velocity model parameterized by Δv. This involves, that the target's TF is captured by the model as present in Y without considering the Doppler effect in the first place. After estimating Δv, a possible Doppler-related scaling of γ can be compensated as discussed in Section IV-C2.

Next, we define suitable models for γ and $\hat{\alpha}$.

A. Target Frequency Transfer Function

We model the characteristic delay-dispersive signature of a target by an FIR structure. We represent this structure by a smooth estimate of the target's TF. The only prerequisite is that the signature has a limited width in time domain, allowing to describe the smooth frequency TF by a small number of sinc functions. The sinc functions are centered at equidistantly spaced frequencies such that the model for a single target response γ_p is formulated as

$$\gamma_p(f) = \sum_{s=1-N_e}^{N_s+N_e} \gamma_{\mathrm{ps}} \cdot \mathrm{sinc}\left(\frac{f}{\Delta S} - s + 0.5\right)\,, \tag{II.4}$$

where $\mathrm{sinc}(x) = \sin(\pi x)/\pi x$ with $\mathrm{sinc}(0) = 1$ and $N_s \in \mathbb{N}$. Additionally, we introduce a model-based bandwidth extension denoted by $N_e \in \mathbb{N}_0$ to mitigate boundary effects at the edges of the spectrum. This in analyzed in Section IV-B. Each sinc function is scaled by a constant complex weight γ_{ps}.

Considering the model for γ one identifies two implications. Firstly, we perform a compression in frequency domain by only estimating $N_s + 2N_e$ amplitudes of the sinc functions instead of a dense frequency sampling. Secondly, the model provides a continuous and smooth representation of the transfer function. This process requires that γ is limited in time domain to an

interval of size T_s. This limit is directly related by $T_s = 1/\Delta S$ to the sinc function spacing ΔS which represents the frequency resolution of the model. This relationship is due to the fact that each sinc function is equivalent to a rectangular model window in time domain with a width of T_s. Due to this fact, a prior assumption about the maximum time extension of γ is required.

B. Velocity and Doppler Model

The velocity and Doppler model can be derived from physics as in [8]. The model for $\hat{\alpha}$ reads as

$$\hat{\alpha}(f, \Delta v) = \frac{\Delta v}{c} \cdot (f + f_c)\,. \tag{II.5}$$

This reveals that $\hat{\alpha}$ is affine linear in f with proportionality constant Δv. The speed of light is denoted by c and f_c is the mixing frequency employed for down mixing to baseband[1]. The physical meaning of Δv is to model a time-variant delay $\tau(t) = \tau - t \cdot \Delta v/c$. It is not equal to the absolute target velocity but the sum of its radial components relative to transmitter and receiver. In case of a monostatic radar the radial target velocity towards the radar is given by $v = \Delta v/2$. For the relation (II.5) to hold, we need to assume $\Delta v \ll c$. Additionally, we slightly modify (II.5) by the following substitution [8]

$$\alpha = \frac{\Delta v}{c} \cdot f_c \tag{II.6}$$

to

$$\hat{\alpha}(f, \alpha) = (f \cdot f_c^{-1} + 1)\alpha\,. \tag{II.7}$$

This allows a significant interpretation. Whenever it holds that $\max(f) \ll f_c$, i.e., the signal covers a small bandwidth compared to the carrier frequency, the frequency-dependence and, hence, Doppler scaling is negligible and the model is dominated by the Doppler shift. If the bandwidth is not sufficiently small, $\hat{\alpha}(f, \alpha)$ accounts for a time-frequency coupling by introducing a time-dependent linear phase in the exponential in (II.3) besides the Doppler shift. This reveals that the model is most important for systems with high relative bandwidths, i.e., UWB systems. In the following, we consider α from (II.6) as a parameter implicitly estimating Δv by (II.7).

C. Discretized Model

To formulate a discrete observation model, we define a uniformly sampled version of S over frequency and time. We define these samples as $S_{ij} = S(f_i, t_i)$ with

$$\begin{aligned} f_i &= f_0 + \Delta f \cdot i \\ t_j &= t_0 + \Delta t \cdot j \\ \text{for} \quad i &= 1, \ldots, N_f \quad \text{and} \quad j = 1, \ldots, N_t\,, \end{aligned} \tag{II.8}$$

where $\Delta f > 0$ and $\Delta t > 0$ are the sampling intervals in frequency and time, respectively, and $N_f, N_t \in \mathbb{N}$ are the numbers of acquired samples.

[1]The Doppler shift depends on the frequency of the actual propagated and modulated signal. Therefore, (II.5) contains $f + f_c$.

Summarizing, using (II.3), (II.7) and (II.4) our discrete model results in $\mathbf{S} \in \mathbb{C}^{N_f \times N_t}$ whose elements S_{ij} are defined as

$$\begin{aligned} S_{ij}(\boldsymbol{\gamma}, \boldsymbol{\tau}, \boldsymbol{\alpha}) = &\sum_{p=1}^{P} \exp\left(-\jmath \cdot 2\pi \cdot f_i \cdot \tau_p\right) \\ &\cdot \exp\left(\jmath \cdot 2\pi \cdot (f_i/N_f \cdot f_r + 1) \cdot t_j \cdot \alpha_p\right) \\ &\cdot \sum_{s=1-N_e}^{N_s+N_e} \gamma_{\mathrm{ps}} \cdot \operatorname{sinc}\left(\frac{f_i}{\Delta S} - s + 0.5\right)\,, \end{aligned} \tag{II.9}$$

where $\boldsymbol{\gamma} = (\gamma_{ps}) \in \mathbb{C}^{P \times N_s + 2 \cdot N_e}$, $\boldsymbol{\tau} \in \mathbb{R}^P$, and $\boldsymbol{\alpha} \in \mathbb{R}^P$. In the following section, we describe how we can estimate the model parameters $\boldsymbol{\gamma}, \boldsymbol{\tau}, \boldsymbol{\alpha}$ from measured data by means of a ML estimator. For the ease of implementation we consider the normalization $f_i \in [-N_f/2,\ N_f/2 - 1]$ and $t_i \in [0,\ N_t - 1]$ such that $\tau_p \in [0,\ 1]$ and $\alpha_p \in [-0.5,\ 0.5]$. Consequently, $f_r = N_f \Delta f / f_c$ represents the relative bandwidth.

III. Maximum Likelihood Estimator

In order to make use of the proposed data model, we have to develop an estimator which is able to extract the parameters from noisy data. This problem can be split up in three intertwined estimation sub-problems. The first is to gain a reasonable estimate of the number of targets present in the observed time-variant transfer function. Additionally, one has to find their parameters as demanded by our data model. Finally, we also have to account for possible measurement noise and stochastic components of the observation and we have to estimate the corresponding distributions.

In this publication, we focus on modeling and estimation of the target's parameters, for which, as a baseline, we draw inspiration from the RIMAX algorithm in [46] and aim to provide an approach for delay-dispersive target responses and velocities that can be viewed as an extension of it. For the sake of clarity, we denote the original RIMAX algorithm and it's applications as the *narrowband case* where, e.g., the velocity can be estimated from the Doppler shift. In contrast, the contributions of this publication target at the *(ultra-)wideband case*.

The main computational obstacle of the wideband data model is the coupling of frequency and time by the Doppler model, which is made indispensable by large relative bandwidths. These changes of the data model with respect to [46] have to be accounted for in the estimation procedure.

A. Statistical Model for the Observations

To formulate a suitable statistical model for our proposed approach, we assume that an observation consists of the superposition of $P \in \mathbb{N}$ distinct target responses for which we can make use of the data model in (II.9) and its discretized version (II.1). Hence, an observation $\mathbf{Y} \in \mathbb{C}^{N_f \times N_t}$ follows

$$\mathbf{Y} = \mathbf{S}(\boldsymbol{\gamma}, \boldsymbol{\tau}, \boldsymbol{\alpha}) + \mathbf{N}\,, \tag{III.1}$$

where $\boldsymbol{N} \in \mathbb{C}^{N_f \times N_t}$ is a random vector representing measurement noise at the sampled frequencies and time instances. In our case, we assume that the entries of $\boldsymbol{N}$ are independent and identically distributed (iid) according to a zero-mean circulary

symmetric complex Gaussian distribution with noise variance σ^2. Accordingly, each observation $\boldsymbol{Y}$ is a complex Gaussian random variable with mean $\mathbf{S}(\boldsymbol{\gamma}, \boldsymbol{\tau}, \boldsymbol{\alpha})$ and identity covariance scaled by σ^2.

Based on these assumptions, the objective is to estimate $P \in \mathbb{N}$, $(\boldsymbol{\gamma}, \boldsymbol{\tau}, \boldsymbol{\alpha}) \in \mathbb{C}^{N_s+2N_e \times P} \times \mathbb{R}^P \times \mathbb{R}^P$ and also $\sigma > 0$ from an observation $\mathbf{Y}$.

B. Maximum Likelihood Estimation

One popular approach for determining parameters from noisy observations is the principle of maximum likelihood estimation. Given the assumed statistical model in (III.1) following a Gaussian distribution, we can formulate the negative log-likelihood function λ, given a certain observation $\mathbf{Y}$, as

$$\lambda(\boldsymbol{\gamma}, \boldsymbol{\tau}, \boldsymbol{\alpha}) = N_f \cdot N_t \cdot \sigma^2 + \sigma^{-2} \cdot \|\mathbf{Y} - \mathbf{S}(\boldsymbol{\gamma}, \boldsymbol{\tau}, \boldsymbol{\alpha})\|_{\mathrm{F}}^2 \,. \quad \text{(III.2)}$$

In order to extract the ML estimate $(\hat{\boldsymbol{\gamma}}, \hat{\boldsymbol{\tau}}, \hat{\boldsymbol{\alpha}})$ one has to determine the global minimum of λ. A necessary condition for minimality is that the score-function $\boldsymbol{J}\lambda$ vanishes at $(\hat{\boldsymbol{\gamma}}, \hat{\boldsymbol{\tau}}, \hat{\boldsymbol{\alpha}})$ [47, Ch. 9.2]. The score-function is the first-order derivative of λ defined as $\boldsymbol{J}\lambda : \mathbb{C}^{P \times N_s + 2N_e} \times \mathbb{R}^P \times \mathbb{R}^P \to \mathbb{C}^{P \times N_s + 2N_e} \times \mathbb{R}^P \times \mathbb{R}^P$ and given by

$$\boldsymbol{J}\lambda(\boldsymbol{\gamma}, \boldsymbol{\tau}, \boldsymbol{\alpha}) = (\boldsymbol{J}_{\boldsymbol{\gamma}}\lambda, \boldsymbol{J}_{\boldsymbol{\tau}}\lambda, \boldsymbol{J}_{\boldsymbol{\alpha}}\lambda)(\boldsymbol{\gamma}, \boldsymbol{\tau}, \boldsymbol{\alpha}) \,. \quad \text{(III.3)}$$

Also, at the optimum, the so-called Fisher Information Matrix (FIM) $\boldsymbol{F}$, which is a positive semi-definite matrix, represents the expectation of the curvature of λ and is defined by

$$\boldsymbol{F}(\boldsymbol{\gamma}, \boldsymbol{\tau}, \boldsymbol{\alpha}) = \boldsymbol{E}\left[\boldsymbol{J}^2\lambda(\boldsymbol{\gamma}, \boldsymbol{\tau}, \boldsymbol{\alpha})\right] \,. \quad \text{(III.4)}$$

Given the assumption that $\mathbf{Y}$ is following a Gaussian distribution, we can analytically calculate $\boldsymbol{F}$ via the Slepian-Bangs formula [48] given by

$$\boldsymbol{F}(\boldsymbol{\gamma}, \boldsymbol{\tau}, \boldsymbol{\alpha}) = -2\Re\left\{\overline{\boldsymbol{J}\boldsymbol{S}(\boldsymbol{\gamma}, \boldsymbol{\tau}, \boldsymbol{\alpha})} \cdot \boldsymbol{J}\boldsymbol{S}(\boldsymbol{\gamma}, \boldsymbol{\tau}, \boldsymbol{\alpha})\right\} \,. \quad \text{(III.5)}$$

Both quantities turn out to be vital components during the development of an algorithm that finds minimizers of the negative log-likelihood as outlined in Section III-C2.

The optimization problem posed by ML is inherently hard to solve, since the objective function is non-convex, so a global minimizer exploiting the smoothness of λ will only converge to a local minimum, which not necessarily is a global optimum. Hence, we have to find a practically and computationally feasible approximation of an ML estimator. The following sections will first explain the approach taken to formulate such an estimator in the narrowband case. Then, we use this as a baseline to extend it to the considered wideband case.

C. Narrowband Iterative ML

For the arguably simpler case of a narrow bandwidth, the ML estimator presented in [15] can make use of several algorithmic simplifications that result from the corresponding narrowband assumptions. These include specular reflections at point-like targets enabling propagation paths between transmitter and receiver as well as a narrowband Doppler model only considering a Doppler shift. Due to this assumptions the model for an observation may be simplified to

$$\tilde{\mathbf{S}}(\tilde{\boldsymbol{\gamma}}, \tilde{\boldsymbol{\tau}}, \tilde{\boldsymbol{\alpha}}) = \sum_p^P \tilde{\gamma}_p \cdot \exp(-\jmath \cdot 2\pi \cdot \tilde{\tau}_p \cdot f_i) \cdot \exp(\jmath \cdot 2\pi \cdot \tilde{\alpha}_p \cdot t_j) \,, \quad \text{(III.6)}$$

with weight $\tilde{\boldsymbol{\gamma}} \in \mathbb{C}^P$. One of the properties of $\tilde{\mathbf{S}}$ is that the parameters $\tilde{\boldsymbol{\tau}}$ and $\tilde{\boldsymbol{\alpha}}$ are decoupled in the sense that they appear in distinct sampled and complex exponentials and hence influence distinct data dimensions, namely frequency and time. This decoupling is realized algebraically by the use of the Kronecker or outer product to form the model for a single propagation path in (III.6). In the following, we will use a $\tilde{\cdot}$ to mark quantities related to the narrowband case.

Similarly as before, we can define the negative log-likelihood function based on $\tilde{\mathbf{S}}$ via

$$\tilde{\lambda}(\tilde{\boldsymbol{\gamma}}, \tilde{\boldsymbol{\tau}}, \tilde{\boldsymbol{\alpha}}) = N_f \cdot N_t \cdot \sigma^2 + \sigma^{-2} \cdot \left\|\mathbf{Y} - \tilde{\mathbf{S}}(\tilde{\boldsymbol{\gamma}}, \tilde{\boldsymbol{\tau}}, \tilde{\boldsymbol{\alpha}})\right\|_F^2 \,. \quad \text{(III.7)}$$

Also, we can define the score function $\tilde{\lambda}$ and the FIM $\tilde{\boldsymbol{F}}$ similarly as before. The RIMAX algorithm works with the model $\tilde{\mathbf{S}}$ and the respective likelihood $\tilde{\lambda}$ and consists of four main building blocks. A global search step [46, Ch. 5.1.5], where a single path is added to the model, a local search procedure [46, Ch. 5.2], where currently found parameters are refined iteratively by a second-order smooth optimizer, an estimator for the noise distribution [46, Ch. 6] and finally a method for removing unreliable paths from the model [46, Ch. 5.2.7.], based on their estimation variance.

As we will see below, the only step that needs substantial changes is the global search for a new path—in our case more precisely for a new target—and how to refine it after inclusion into the model. To motivate these changes, we briefly describe the approach of the algorithm in [46] that works with the narrowband models in (III.6) and (III.7).

On the highest level of abstraction, the RIMAX algorithm iteratively increases the model complexity, i.e., increases P until no more reliable paths can be added. Hence, the first problem one encounters is to find a suitable initial guess for the parameters of a newly added path. A good initial guess in step k is found, if the resulting parameter tuple $(\tilde{\boldsymbol{\gamma}}^k, \tilde{\boldsymbol{\tau}}^k, \tilde{\boldsymbol{\alpha}}^k) \in \mathbb{C}^k \times \mathbb{R}^k \times \mathbb{R}^k$ is close enough to the optimum such that the objective $\tilde{\lambda}$ is locally convex and the region of convexity contains the global minimum. In this case, a local optimizer initialized with $(\tilde{\boldsymbol{\gamma}}^k, \tilde{\boldsymbol{\tau}}^k, \tilde{\boldsymbol{\alpha}}^k)$ can recover the optimum given this initial guess.

1) Narrowband Path Search: The approach presented in [46] essentially implements a grid-based and sequentially executed matched filter, which makes use of the Kronecker structure in (III.6). To describe this method, we define $\boldsymbol{a}_f : \mathbb{R} \to \mathbb{C}^{N_f}$ and $\boldsymbol{a}_t : \mathbb{R} \to \mathbb{C}^{N_t}$ as

$$\begin{aligned} \boldsymbol{a}_f(\tau) &= \exp(-\jmath \cdot 2\pi \cdot \tau \cdot f) \quad \text{(III.8)} \\ \boldsymbol{a}_t(\alpha) &= \exp(\jmath \cdot 2\pi \cdot \alpha \cdot t) \,. \end{aligned}$$

Next, we define two sets of grid points $G_f = \{i/N_f \mid i = 0, \ldots, N_f - 1\}$ and $G_t = \{i/N_t - 1/2 \mid i = 0, \ldots, N_t - 1\}$ to define the matrices $\boldsymbol{A}_f \in \mathbb{C}^{N_f \times N_f}$ and $\boldsymbol{A}_t \in \mathbb{C}^{N_t \times N_t}$ as

$$\boldsymbol{A}_f = [\boldsymbol{a}_f(\tau)]_{\tau \in G_f} \quad \text{and} \quad \boldsymbol{A}_t = [\boldsymbol{a}_t(\alpha)]_{\alpha \in G_t} \,. \quad \text{(III.9)}$$

Now assume in step k we already have a previous estimate $(\tilde{\boldsymbol{\gamma}}^{k-1}, \tilde{\boldsymbol{\tau}}^{k-1}, \tilde{\boldsymbol{\alpha}}^{k-1})$ at our disposal. Then, the so-called residual in step $k-1$ can be defined via

$$\tilde{\mathbf{R}}^{k-1} = \boldsymbol{Y} - \tilde{\mathbf{S}}(\tilde{\boldsymbol{\gamma}}^{k-1}, \tilde{\boldsymbol{\tau}}^{k-1}, \tilde{\boldsymbol{\alpha}}^{k-1}) \,. \quad \text{(III.10)}$$

To find a new tuple $(\tilde{\tau}, \tilde{\alpha})$ we first find the index i_f, which picks out the maximum element i_f in the non-negative vector

$$\boldsymbol{c}_f = \left|\boldsymbol{A}_f^H \cdot \tilde{\mathbf{R}}^{k-1}\right|^2 \cdot \mathbf{1}_{N_f} \in \mathbb{C}^{N_f} \,. \quad \text{(III.11)}$$

Algorithm 1 Processing flow to find a set of parameters after $k-1$ steps.

Calculate $\tilde{\mathbf{R}}^{k-1}$ acc. to (III.10).
Use (III.11), (III.12) and (III.13) to find $\tilde{\boldsymbol{\tau}}^k$ and $\tilde{\boldsymbol{\alpha}}^k$.
Calculate $\tilde{\boldsymbol{\gamma}}^k$ by means of least-squares using (A.1).

Algorithm 2 Processing flow to find a net set of parameters after $k-1$ steps.

Calculate $\mathbf{R}^{k-1}$ acc. to (III.15).
Use (III.11), (III.12) and (III.13) to find $\tilde{\boldsymbol{\tau}}^k$ and $\tilde{\boldsymbol{\alpha}}^k$.
Calculate $\boldsymbol{\gamma}^k$ by means of least-squares given by (A.2).

Based on i_f we calculate the so-called beamformed residual

$$\boldsymbol{r}_f^k = \boldsymbol{a}_f(i_f/N_f)^H \cdot \tilde{\mathbf{R}}^{k-1} \in \mathbb{C}^{N_t}\,. \tag{III.12}$$

Then, we find the index i_t, which picks out the maximum entry in

$$\boldsymbol{c}_t = \left|\boldsymbol{A}_t^H \cdot \boldsymbol{r}_f^k\right|^2 \in \mathbb{C}^{N_t}\,, \tag{III.13}$$

in order to finally derive the grid-based matched filter estimate via

$$(\tilde{\tau}^k, \tilde{\alpha}^k) = (i_f/N_f, i_t/N_t - 1/2)\,.$$

As a last step, we append $\tilde{\tau}^k$ and $\tilde{\alpha}^k$ to $\tilde{\boldsymbol{\tau}}^{k-1}$ and $\tilde{\boldsymbol{\alpha}}^{k-1}$ respectively to form $\tilde{\boldsymbol{\tau}}^k$ and $\tilde{\boldsymbol{\alpha}}^k$ and find the path weights $\tilde{\boldsymbol{\gamma}}^k$ by means of least-squares as given in (A.1). The methodology is summarized in Algorithm 1.

The main observation to make is that the steps (III.11), (III.12) and (III.13) are only valid, since the parameters $\tilde{\tau}$ and $\tilde{\alpha}$ influence distinct data dimensions due to the narrowband assumption. Hence, the matched filter output can be computed efficiently with $\mathcal{O}(N_f^2 \cdot N_t + N_t^2)$ floating point operations. In contrast, $\mathcal{O}(N_f^2 \cdot N_t^2)$ operations would have been necessary, if we evaluated the grid for the two parameters jointly. Note that in [46, Ch. 5.1.2.] the algorithm is explained in much more generality such that it also applies to a multiple input multiple output (MIMO)-channel observation.

2) Narrowband Parameter Refinement: In order to mitigate the resolution limit imposed upon the global search procedure using G_f and G_t the RIMAX algorithm executes SAGE [49] for all paths currently existing in the model each time a new path is added. Since SAGE only optimizes the parameters $(\tilde{\gamma}, \tilde{\tau}, \tilde{\alpha})$ for a single propagation path while keeping the others fixed, its computational cost is similar to that of Algorithm 1. Additionally, [49] presents some convergence criteria, which makes SAGE a valid approach from an estimation perspective.

Once all required new paths are added by means of Algorithm 1 and SAGE, a second-order and joint optimization of the whole set of path parameters is carried out by

$$\begin{aligned}(\tilde{\boldsymbol{\gamma}}^{k,\ell+1}, \tilde{\boldsymbol{\tau}}^{k,\ell+1}, \tilde{\boldsymbol{\alpha}}^{k,\ell+1}) = (\tilde{\boldsymbol{\gamma}}^{k,\ell}, \tilde{\boldsymbol{\tau}}^{k,\ell}, \tilde{\boldsymbol{\alpha}}^{k,\ell}) \\ - \varepsilon \cdot \tilde{\boldsymbol{F}}^{-1} \cdot \boldsymbol{J}\tilde{\lambda}(\tilde{\boldsymbol{\gamma}}^{k,\ell}, \tilde{\boldsymbol{\tau}}^{k,\ell}, \tilde{\boldsymbol{\alpha}}^{k,\ell})\,,\end{aligned} \tag{III.14}$$

which constitutes the so-called Fisher-scored gradient method [50] with step size ε, where the steepest descent-direction is corrected according to the knowledge of the curvature at the current point of iteration. The iteration is denoted by ℓ. This algorithm has good convergence properties and comes at moderate computational cost, since no second order derivatives are necessary. At this point we are in the place to formulate the algorithmic scheme adapted to our proposed data model.

The important thing to notice is that for our purposes it makes no difference if the iteration in (III.14) is executed based on $\tilde{\mathbf{S}}$ and $\tilde{\lambda}$ or on $\mathbf{S}$ and λ using the respective score functions and FIMs. Further, the computational complexity of $\mathbf{S}$ may be increased compared to $\tilde{\mathbf{S}}$, but not as substantially as the complexity of the search for a new path—or more specifically a new target target—over the joint grid for τ and α. To retain the algorithmic advantages, the main idea of the wideband estimator is to use the initialization presented in Algorithm 1 with a slight modification.

To this end, we define the residual similarly to (III.10) via

$$\mathbf{R}^{k-1} = \boldsymbol{Y} - \mathbf{S}(\boldsymbol{\gamma}^{k-1}, \tilde{\boldsymbol{\tau}}^{k-1}, \tilde{\boldsymbol{\alpha}}^{k-1})\,. \tag{III.15}$$

Once we have established an initial estimate based on $\tilde{\mathbf{S}}$, we replace the model by $\mathbf{S}$ while keeping the parameters $(\tilde{\boldsymbol{\tau}}^{k-1}, \tilde{\boldsymbol{\alpha}}^{k-1})$ fixed and determine $\boldsymbol{\gamma}^{k-1}$ by means of least-squares now based on $\boldsymbol{S}$. Then we carry out the steps in (III.11), (III.12), and (III.13) based on this wideband residual instead of the narrowband instance $\tilde{\mathbf{R}}$ to obtain estimates for $(\tilde{\tau}^k, \tilde{\alpha}^k)$. This is outlined in Algorithm 2. In this way we have avoided using the wideband data model, where delay and Doppler are inherently coupled and have circumvented the joint 2D path search. The parameter refinement with SAGE, however, is performed on the joint 2D grid.

Once this initial estimate for $(\boldsymbol{\gamma}^k, \boldsymbol{\tau}^k, \boldsymbol{\alpha}^k)$ is established, we update it according to

$$\begin{aligned}(\boldsymbol{\gamma}^{k,\ell+1}, \boldsymbol{\tau}^{k,\ell+1}, \boldsymbol{\alpha}^{k,\ell+1}) = (\boldsymbol{\gamma}^{k,\ell}, \boldsymbol{\tau}^{k,\ell}, \boldsymbol{\alpha}^{k,\ell}) \\ - \varepsilon \cdot \boldsymbol{F}^{-1} \cdot \boldsymbol{J}\lambda(\boldsymbol{\gamma}^{k,\ell}, \boldsymbol{\tau}^{k,\ell}, \boldsymbol{\alpha}^{k,\ell})\,,\end{aligned} \tag{III.16}$$

which is the wideband and hence more complex version of (III.14). However, we only need to evaluate the model $\boldsymbol{S}$ for the currently found k-paths, which results only in a mild increase in computational complexity for $\boldsymbol{S}$ compared to $\tilde{\boldsymbol{S}}$. Both procedures are summarized in Figure 1 to visualize the differences.

D. Computational Aspects

The iteration in (III.16) is usually paired with a stopping criterion that evaluates the relative changes of the likelihood function λ. Hence, in total, the necessary quantities that need to be computed efficiently are the likelihood λ and hence also its main building block $\mathbf{S}$.

For the gradient iteration we directly need access to $\boldsymbol{J}\lambda$, which also makes $\boldsymbol{J}\mathbf{S}$ a quantity necessary to compute. Finally, to employ the correction by means of the inverse FIM we see that by computing $\boldsymbol{J}\mathbf{S}$ we have already overcome the largest computational obstacle for $\boldsymbol{F}$.

E. Model Order Selection and Noise Estimation

Although the data model of the proposed estimator is inherently different than the one presented in [46, Ch. 5.2.7], we have made straightforward modifications to the algorithm such that the methods for both presented therein are directly applicable to our case.

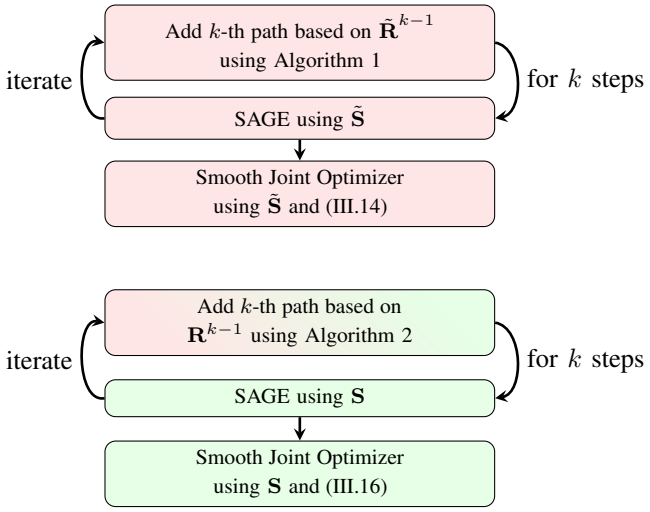

Fig. 1: Processing diagram of RIMAX [46] (top) in comparison to the proposed wideband ML estimator (bottom). The color gradient highlights that the wideband path search is partially based on the narrowband model.

The following section will study various effects and ramifications of the proposed data model and estimator.

IV. Numerical Evaluations

In this section, we analyze the proposed model and estimator from a numerical point of view and provide examples and visualizations. After introducing the simulation of the dispersive target responses, we discuss the implications of the wideband model. Additionally, we compare our approach to state of the art algorithms, i.e., RIMAX [46] in original form and a piece-wise frequency-flat subband approach as proposed in [6] or [45]. Furthermore, we analyze a limitation of the approach and conclude the section by a discussion about two different aspects of the Doppler effect.

Whenever we visualize the time or Doppler domain we compute a FFT utilizing a Hanning window over frequency or (slow) time. Additionally, we average over the not-visualized data dimension.

A. Description of the Simulation

We simulate a multi-target response. Each individual target is modeled as extended in a way that it is represented by a cluster of specular reflections of closely spaced scattering centers. Each cluster is based on the narrowband model from (III.6) such that the full simulation model results in

$$Y_{ij} = \sum_{p}^{P} \sum_{q}^{Q} \gamma_{pq} \cdot \exp(-\jmath \cdot 2\pi \cdot \tau_{pq} \cdot f_i) + n_{ij} \,. \tag{IV.1}$$

At this point, we consider a static scenario such that Y is constant over time t. P indicates the number of targets and Q the cluster size, i.e., the number of closely spaced specular components composing a target. The complex amplitude is modeled as

$$\gamma_{pq} = a_{pq} \cdot \exp(\jmath \cdot 2\pi \cdot \varphi_{pq}) \,, \tag{IV.2}$$

where $a_{pq}, \varphi_{pq} \sim \mathcal{U}(0,1)$ are drawn independently from a uniform distribution. The delays $\tau_{pq} \sim \mathcal{N}(\tau_p, \varrho_p^2)$ are drawn independently from a Gaussian distribution whose statistics depend on the target p. The variable τ_p is the global target delay and ϱ_p sets the width of the response. White Gaussian noise with noise power level σ^2 is added by n_{ij}.

To add a dynamic component to the simulation we extent (IV.1) by a velocity model in accordance with (II.9)

$$\begin{aligned} Y_{ij} = \sum_{p}^{P} \sum_{q}^{Q} & \gamma_{pq} \cdot \exp(-\jmath \cdot 2\pi \cdot \tau_{pq} \cdot f_i) \\ & \cdot \exp\left(\jmath \cdot 2\pi \cdot (f_i/N_f \cdot f_r + 1) \cdot t_j \cdot \alpha_p\right) \\ & + n_{ij} \,. \end{aligned} \tag{IV.3}$$

The velocity parameter α varies between targets but is constant for all components composing a target. The static and dynamic simulation parameters are summarized in Table I.

TABLE I: Static (top) and dynamic (bottom) simulation settings for (IV.1) and (IV.3).

Parameter	System	Target 1	Target 2
Frequency samples N_f	1000	-	-
Time samples N_t	10	-	-
Noise power level σ^2	-40dB	-	-
Target delay τ	-	0.1	0.15
Response width ϱ	-	0.0005	0.0020
Cluster size Q	20	-	-
Time samples N_t	40	-	-
Relative bandwidth f_r	0.5	-	-
Target velocity α	-	-0.01	0.2

B. Time-invariant Analyses

Figure 2a displays a section of the simulated and modeled Impulse Response (IR) of the static simulation with (IV.1) and Table I in time domain. One can see that the model fits the simulated data after estimating the optimal parameters. The residual approaches the noise power level σ^2. The model window depicts the time limitation T_s resulting from the finite number of sinc functions composing the individual target TFs. The windows are shifted to the corresponding position by the delay parameters τ_p. The complete TF in Figure 2b does not allow conclusions about the frequency characteristics of the individual targets. Though, the multi-target nature of the wideband model and estimator captures the TF of each target separately as visualized in Figure 2c and Figure 2d. These plots reveal the different target characteristics which can now be analyzed individually. Each TF is approximated by 10 sinc functions spread over the spectrum. To enhance the model fit, we further exploit the fact that the sinc functions are not limited in frequency domain but spread over the whole spectrum. For this, we define overlapping sinc functions specified by $N_e > 0$ in (II.9). This allows to further enhance the model fit especially at the edges of the spectrum. In this way, the model is not purely limited to the observed bandwidth up to a certain degree. The influence of N_e on the estimation of the given TFs is exemplified in Figure 3 where (a) displays the model fit given $N_e = 0$ and (b) the model fit given $N_e = 2$ which is also the setting for Figure 2. A lack of overlapping sinc functions

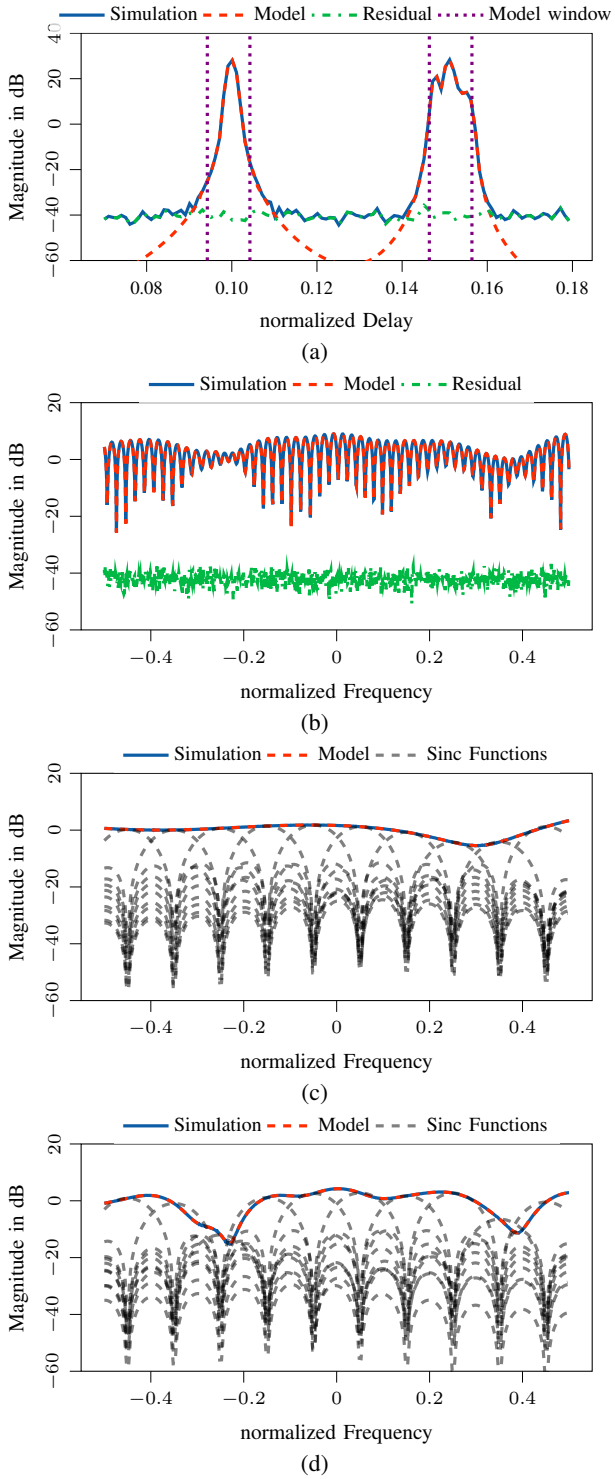

Fig. 2: Comparison of the simulated and modeled signal after parameter estimation. (a) and (b) show the time and frequency domain representation of the complete signal whereas (c) and (d) visualize the simulated and modeled TF of target 1 and 2.

clearly influences the fit within the frequency band resulting in a ripple of the estimated TF. Hence, for wideband target responses, the use of overlapping sinc functions is of great benefit.

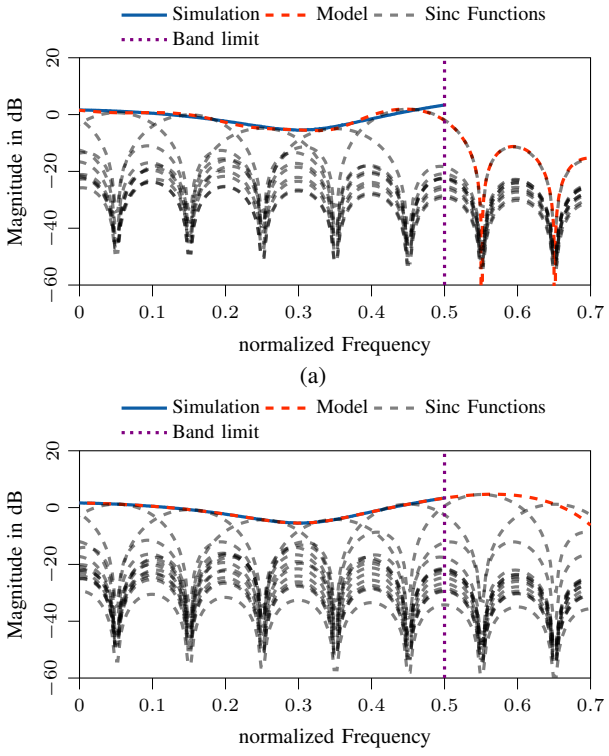

Fig. 3: Section of the TF of target 1 estimated (a) without ($N_e = 0$) and (b) with ($N_e = 2$) overlapping sinc functions.

1) Target Superposition: The nature of the model requires a clear separation of the Impulse Responses (IRs) of multiple targets in the parameter domains, either in delay or velocity. If such a separation is not given, the model can only capture the superposition of the individual target responses and the estimator wrongly estimates a single target.

To analyze the transition from two targets wrongly estimated as a single one to a clear separation, we perform numerical experiments with the simulations from (IV.1) and Table I. The second target is varied in its τ parameter starting from an overlap with target 1 ($\tau_2 = 0.1$) up to a clear separation ($\tau_2 = 0.15$). For each τ_2, we perform 10 experiments with independent noise realizations and average the residuals accordingly.

Figure 4 displays the residual of the data model fit. The x-axis represents the varying τ_2 parameter and hence the distance $\Delta\tau$ between the targets. It is normalized to the model window T_s. For the ease of interpretation, $\overline{\varrho} = (\varrho_1 + \varrho_2)/2$ is added to $\Delta\tau$, since the target IRs have a certain width and hence, the actual distance is accordingly smaller. The y-axis displays the global mean squared residual as well as the residuals between each target estimate and the corresponding simulated TF.

For small distances within the model window T_s, both signals can be captured by a single target model. Therefore, the global residual is at the noise level, though, the residual of target 1 is quite large since it captures the superposition of both targets. When the distance gets close to the model window, the width of the superimposed IR exceeds T_s and cannot be captured by a single model component anymore. However, adding a second

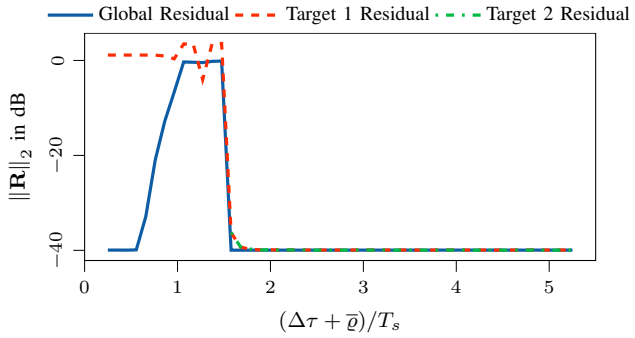

Fig. 4: Estimation residuals for a two target scenario evaluated over a varying distance in delay between the targets.

target to the model leads to unreliable parameter estimates and is hence omitted by the estimator. This is due to the fact, that the model for the first target is not placed exactly at parameter τ_1 but at a different position where it fits best to the superimposed IR and maximizes the likelihood the most. Adding a second target will then lead to an overlap of the two model windows. After increasing the distance further, both target models can be placed in a way that each model describes an individual simulated target. Then, all three residuals drop to the noise level resulting in a good concordance between model and data.

The experiments reveal that the proposed model cannot distinguish between an individual target response or a superposition of several responses if they are not separated in the considered parameter domains. A decomposition into individual model components will fail, e.g., if several targets in a static scenario are distributed over the angular domains but share the same distance to the radar system. For a separation, model and estimator would need to consider the angular domains.

2) Comparison to RIMAX: In Section III we already discussed the similarities and differences between the RIMAX algorithm and the proposed wideband extensions. In this section, we want to investigate the claim of the introduction that such a point-like target model is indeed able to capture delay-dispersive response at the expense of resulting in a number of individual and unrelated model components. Therefore, we apply RIMAX to target 2 from the previous simulation (see Table I and (IV.1)). The results are visualized in Figure 5a and Figure 5b and visually resemble the results from the wideband model in Figure 2a and Figure 2d. As model order, 10 paths are estimated whose delay parameters are highlighted in Figure 5a by vertical lines. The total number of free model parameters for the RIMAX solution sums up to 20 (10-dimensional τ and 10-dimensional γ) and is, hence, sightly higher as for the wideband model with 13 free parameters (1-dimensional τ and (8+4)-dimensional γ).

Nevertheless, the predefinition of the pulse width for the wideband model directly results in the estimation of a single target response. The RIMAX solution does not require such a predefinition. Thereby, the estimated paths do not reveal if they belong to a single or multiple targets. A separation into individual and extended target responses would require a grouping or clustering of the estimated paths as a postprocessing step.

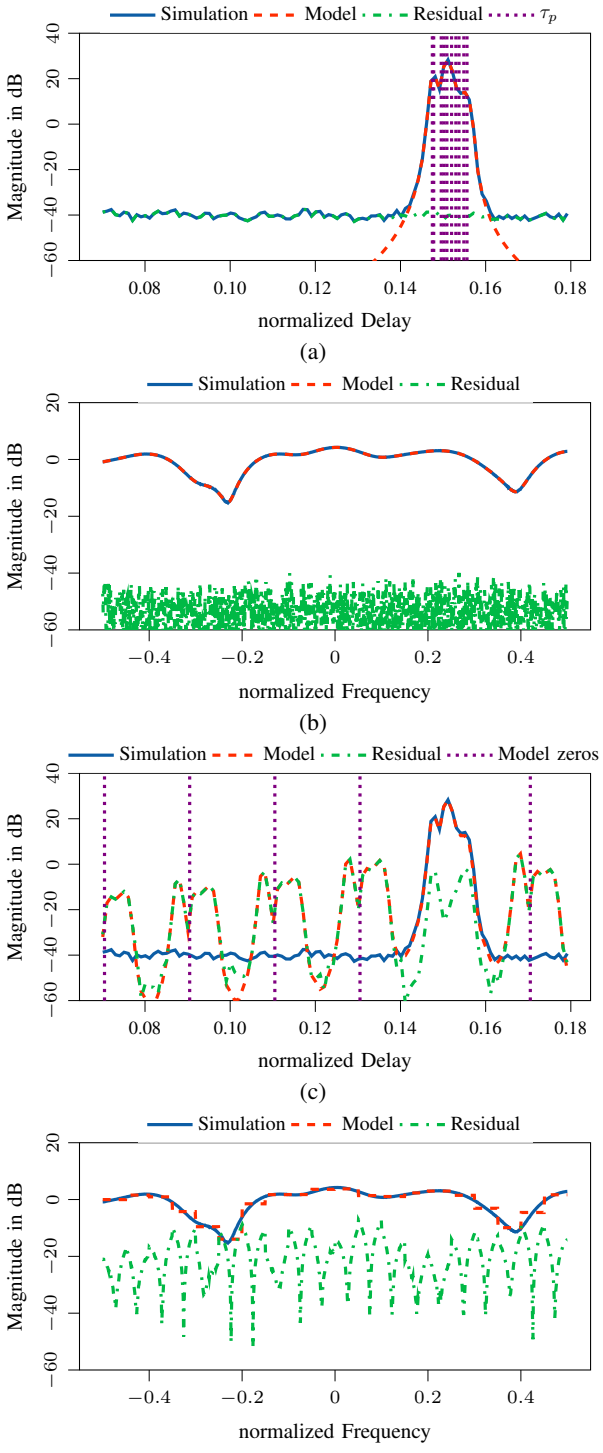

Fig. 5: Comparison of the simulated and different estimated signals using state of the art algorithms. (a) and (b) visualize results of the RIMAX algorithm (Section IV-B2) with 10 individual paths. (c) and (d) display the results of the constant subband model (Section IV-B3) with 20 subbands.

3) Comparison to a Constant Subband Model: Instead of modeling the dispersive target response by a superposition of

specular components (Section IV-B2), one could approximate the target's frequency TF by decomposing the wideband spectrum into N_s *narrow bands*, i.e., piece-wise frequency-flat subbands. This is comparable to the approaches in [6], [44], [45]. In our experiment, each of these subbands has its own complex amplitude γ_{ps} as model parameter, whereas τ is constant over all subbands. This is closely related to the proposed wideband model in (II.4), by replacing the sinc functions with rectangular functions as

$$\gamma_p(f_i) = \sum_{s=1}^{N_s} \gamma_{\mathrm{ps}} \cdot \mathrm{rect}\left(\frac{f_i}{\Delta S} - s + 0.5\right) , \qquad \text{(IV.4)}$$

with

$$\mathrm{rect}(x) = \begin{cases} 0 & |x| > 0.5 \\ 1 & |x| \leq 0.5 \end{cases} . \qquad \text{(IV.5)}$$

The TF is parameterized by $\boldsymbol{\gamma} = (\gamma_{ps}) \in \mathbb{C}^{P \times N_s}$ and the width of each subband is given by $\Delta S > 0$.

Figure 5c and Figure 5d show exemplary results for $N_s = 20$ for target 2 of the simulation (see Table I and (IV.1)). The frequency plot reveals the step-like approximation of the spectrum which leads to a noticeable structure in the residual rising at each transition between two consecutive subbands.

This deterministic structure of the residual also has side-effects on the time domain, namely the generation of sidelobes in the model as exemplified in Figure 5c. The position of the sidelobes can be directly inferred from (IV.4). The rectangular subbands in frequency domain correspond to a superposition of sinc functions in time domain, each centered at the common delay τ_p. The sinc functions have the same zeros located at $\tau_p \pm {}^{k}/_{\Delta S}$ with $k \in \mathbb{N}$ as marked in the figure. At those locations, the superposition of the sinc functions results in a deterministic model error rendering the time domain representation of this model unusable. Although using a comparable amount of free model parameters which sum up to 21 (1-dimensional τ and 20-dimensional γ), the subband model performs poorly in a qualitative comparison to the proposed wideband model (Section IV-B) and the RIMAX algorithm (Section IV-B2).

C. Time-variant Analyses

When it comes to time-variant scenarios, two aspects of the Doppler effect have to be considered. On the one hand, Doppler influences the signal modulation over (slow) time as already discussed in Section II-B. Given a high relative bandwidth, the modulation is caused by a scaling of the signal's spectrum. This effect is already incorporated into the proposed dispersive model in (II.9). On the other hand, the observed target TF γ over frequency (or fast time) will also be subject to the Doppler effect. The latter will be discussed in Section IV-C2.

The modulation over slow time is exemplary visualized in Figure 6a as Doppler spectrum using simulations from (IV.3) and Table I. The different spreads of the two target responses result from the velocity dependent Doppler scaling. Since this scaling is incorporated into the model, both targets can be described by the scalar parameter α which is directly related to a velocity by (II.6).

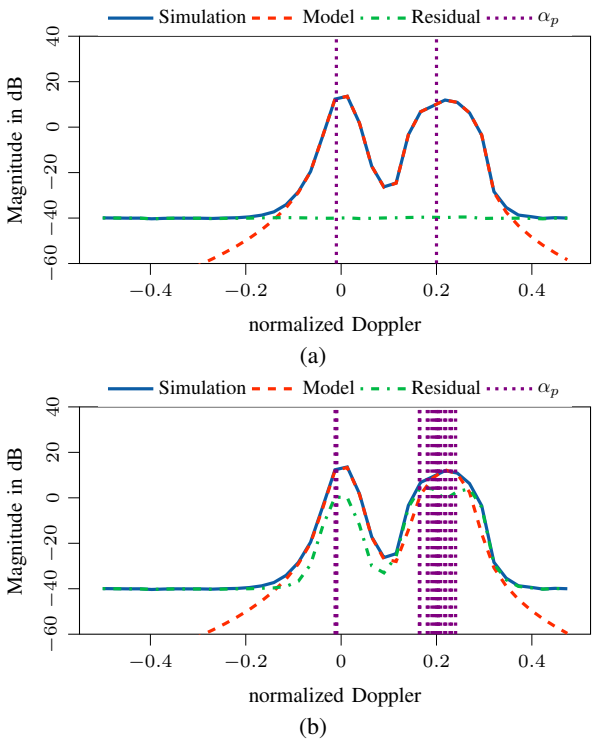

Fig. 6: Comparison of the simulated and different estimated signals in Doppler domain using (a) the proposed wideband model and (b) a model based on a pure Doppler shift.

1) Comparison to RIMAX: In contrast to the wideband model, the RIMAX algorithm in original form is build on narrowband assumptions and does only consider a Doppler shift assuming small relative bandwidths. In Section IV-B2 we discussed that a delay-dispersive target response can be captured by the RIMAX algorithm as a superposition of several individual model components. However, the mismatch of the Doppler model for larger relative bandwidths cannot be compensated by a superposition of multiple components as visualized in Figure 6b. As in the example from Figure 5a the algorithm spreads several components (in this case 20) over the Doppler domain. Nevertheless, the residual reveals that the model is not able to fit the simulated data sufficiently. Furthermore, while the decomposition into several delay components is physically justifiable by extended target geometries and individual scattering centers, the decomposition into distributed Doppler components is purely caused by model mismatch and prevents a derivation of the actual target velocity.

Furthermore, the impact of the model mismatch does not only depend on the target's velocity Δv but also on the velocity's relation to the sampling interval in time Δt. Since α is normalized to the sampling frequency $1/\Delta t$, small velocities can already lead to a significant spread in the Doppler spectrum.

2) Doppler Effect on the Target's TF: The observed target TF γ over frequency (or fast time) will also be subject to the Doppler effect which is not yet considered in the models used for the simulations and estimations. Those models are only considering the modulation over (slow) time. To evaluate the influence on fast time, the Doppler effect can be modeled as

a frequency mapping defined by

$$f_i = f_i' + \eta \cdot \hat{\alpha}(f_i', \alpha)\,, \tag{IV.6}$$

where $\hat{\alpha}$ is the normalized and frequency-depended Doppler shift as in (II.7). Hence, (IV.6) describes where a frequency f_i' will be shifted due to the target's velocity represented by α. Since f_i and f_i' are normalized differently than $\hat{\alpha}$ and α, η converts between the two normalizations.

The variable $\alpha \in [-0.5,\ 0.5]$ is normalized to the sampling interval in time Δt such that $\alpha = \pm 0.5$ corresponds to the maximum unambiguous velocity $\pm\Delta v_m$. The Doppler shift in Hz corresponding to α is given by (II.6). Dividing it by Δf converts it to the normalization of f_i since $f_i \in [-N_f/2,\ N_f/2\ -1]$. Hence, η results in

$$\eta = \frac{\Delta v_m}{c} \cdot \frac{2 \cdot f_c}{\Delta f}\,. \tag{IV.7}$$

The factor 2 assures that $\alpha = \pm 0.5$ corresponds to the Doppler shift generated by Δv_m. Using the definition of the relative bandwidth from Section II-C, f_c can be expressed as

$$f_c = \frac{N_f \Delta f}{f_r}\,. \tag{IV.8}$$

Hence, the normalization conversion η reads as

$$\eta = \frac{\Delta v_m}{c} \cdot \frac{2 \cdot N_f}{f_r}\,. \tag{IV.9}$$

Simulation: Given (IV.6) we can simulate Doppler scaled target responses by evaluating the delay exponentials of a target's TF in (IV.3) on a non-uniform frequency grid f_i' such that

$$\begin{aligned} Y_{ij}' = \sum_{p}^{P} \sum_{q}^{Q} & \gamma_{pq} \cdot \exp(-\jmath \cdot 2\pi \cdot \tau_{pq}' \cdot f_i') \\ & \cdot \exp\left(\jmath \cdot 2\pi \cdot (f_i/N_f \cdot f_r + 1) \cdot t_j \cdot \alpha_p\right) \\ & + n_{ij}\,. \end{aligned} \tag{IV.10}$$

Variable f_i' maps the frequency axis $f_i \in [-N_f/2,\ N_f/2-1]$ to the frequency values of the unmodulated target TF, i.e., to the frequencies from where the values at f_i originate. Converting (IV.6) to f_i' yields

$$f_i' = \frac{f_i - \eta \cdot \alpha}{1 + \eta \cdot \alpha \cdot f_r/N_f}\,. \tag{IV.11}$$

Furthermore, the evaluation on the nonlinear frequency grid f_i' leads to an offset of the delay parameter. To keep the delay values from Table I this offset is compensated by adjusting τ_{pq} as

$$\tau_{pq}' = \tau_{pq} + \tau_p \cdot \frac{2 \cdot \alpha \cdot \Delta v_m}{c}\,, \tag{IV.12}$$

with mean cluster delay τ_p.

Finally, to compare the results in this section for a wide range of simulated velocities, we assume that Δv_m is adapted to each experiment such that $\Delta v = 0.4 \cdot \Delta v_m$. Hence, α equals 0.2 for all experiments.

Compensation: The model in (II.9) does not consider a Doppler scaling of the target's TF. Therefore, the TF is observed and estimated in the scaled state and needs to be compensated afterwards. Similar to the simulation we can compensate the Doppler scaling by evaluating the TF-related parts of the model on a nonlinear frequency grid after the actual parameter estimation as

$$\begin{aligned} S_{ij}'(\boldsymbol{\gamma}, \boldsymbol{\tau}, \boldsymbol{\alpha}) = & \sum_{p=1}^{P} \exp\left(-\jmath \cdot 2\pi \cdot f_i'' \cdot \tau_p\right) \\ & \cdot \sum_{s=1-N_e}^{N_s+N_e} \gamma_{\mathrm{ps}} \cdot \mathrm{sinc}\left(\frac{f_i''}{\Delta S} - s + 0.5\right) \\ & \cdot \exp\left(\jmath \cdot 2\pi \cdot f_i \cdot \tau_p \cdot \frac{2 \cdot \alpha \cdot \Delta v_m}{c}\right) \\ & \cdot \exp\left(\jmath \cdot 2\pi \cdot (f_i/N_f \cdot f_r + 1) \cdot t_j \cdot \alpha_p\right)\,. \end{aligned} \tag{IV.13}$$

To acquire the actual target response, f_i'' maps the frequency axis $f_i \in [-N_f/2,\ N_f/2-1]$ to the frequency values of the scaled target TF, i.e., to which frequency f_i has been shifted due to the Doppler effect

$$f_i'' = f_i + \eta \cdot \hat{\alpha}(f_i, \alpha)\,. \tag{IV.14}$$

Similar to the simulation we need to compensate a delay offset, this time after evaluating the model on f_i'' . Hence, we multiply an additional delay exponential to the model in (IV.13).

Evaluation: With the following experiments we evaluate the necessity of a Doppler compensation of the estimated TF. Therefore, we performed two dynamic simulations, one as described in Section IV-A and another one with the modifications from above considering a Doppler scaling over fast time. We use the simulation parameters from Table I for target 2 and identical values drawn from the cluster statistics such that both TFs are identical if no Doppler scaling would be applied over fast time. We consider the previous simulation from Section IV-A as ground truth and the Doppler scaled simulation from this section as input to the parameter estimator. Hence, the estimator estimates the model parameters according to the scaled target TF. Afterwards, we calculate the compensated TF as described above.

For the evaluation, we define two mean-squared errors.

$$E_u = \frac{1}{N_f N_t} \left\| \mathbf{Y} - \mathbf{S}(\boldsymbol{\gamma}, \boldsymbol{\tau}, \boldsymbol{\alpha} \mid \mathbf{Y}') \right\|_F^2 \tag{IV.15}$$

captures the error between the ground truth data and the estimated and uncompensated model given the Doppler simulation from (IV.10) as input.

$$E_c = \frac{1}{N_f N_t} \left\| \mathbf{Y} - \mathbf{S}'(\boldsymbol{\gamma}, \boldsymbol{\tau}, \boldsymbol{\alpha} \mid \mathbf{Y}') \right\|_F^2 \tag{IV.16}$$

captures the error between the ground truth data and the compensated model from (IV.13).

The difference between the two errors $E_u - E_c$ is visualized in Figure 7 over two varying parameters: (1) the target velocity via Δv_m by keeping $\alpha = 0.2$ fixed and (2) the sampling interval Δf, i.e., the frequency resolution of the system. The latter is normalized to f_c such that

$$\frac{\Delta f}{f_c} = \frac{f_r}{N_f}\,. \tag{IV.17}$$

The varying resolution requires that the number of sinc functions N_s is adapted accordingly to keep the size of the model window in time domain fixed. N_s is adapted by

$$N_s = \left\lceil \frac{10}{1000} \cdot N_f \right\rceil\,. \tag{IV.18}$$

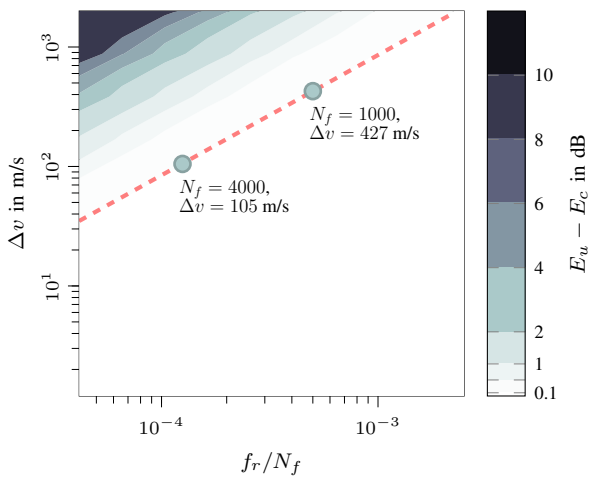

Fig. 7: Deviation between the uncompensated and the compensated model relative to the target's velocity and the system's frequency resolution. The red dashed line highlights the first contour line at 0.1 dB.

The difference $E_u - E_c$ is drawn as colored areas on a dB scale. As expected, the accuracy of the uncompensated model drops for rising target velocities and a rising frequency resolution. In other words, the uncompensated model performs worse if the Doppler shift is significant relative to the frequency resolution of the system. However, for most of the figure the difference stays below 0.1 dB as highlighted by the red dashed line. Below this line, the gain of a Doppler compensation can be considered negligible. Two exemplary data points provide combinations of N_f and Δv which still don't require a Doppler compensation.

We conclude that the necessity of a Doppler compensation over fast time depends on the application and radar system. Hence, we do not incorporate Doppler related terms into the model for the target's TF. This would apparently increase the complexity of the model and estimation routine. If necessary, the Doppler modulation can be compensated as postprocessing step as described in the current section.

V. Measurements

To conclude our investigations we want to validate the model and the estimator on exemplary short-range measurement data acquired with a *m:explore* M-sequence radar from *Ilmsens GmbH* operating in baseband from $0.1 - 6$ GHz. The transmitter and receiver ports are connected to two *DRH20E* ridged horn antennas from *RF SPIN* which are mounted on a stand in horizontal polarization resulting in a quasi-monostatic and single-polarized radar configuration. The Signal-to-Noise Ratio (SNR) of this system effectively limits the usable frequency band to $1.5 - 5.5$ GHz. The radar and signal parameters are summarized in Table II.

The test object—a wooden plate with four metal corners as feet—is placed on Styrofoam in 0.8 cm distance to the antennas. Direct sources of reflections like walls are covered with absorbers, though, measurements have not been performed in an anechoic chamber. Furthermore, we acquire and subtract background measurements without the test object to reduce antenna crosstalk and clutter.

TABLE II: Parameters of the measurement setup.

Parameter	System	Target
Frequency samples N_f	1230	-
Frequency resolution Δf	3.3 MHz	-
Time samples N_t	10	-
Time resolution Δt	25 ns	-
Maximum range	46 m	-
Range resolution	3.8 cm	-
Frequency band	$1.5 - 5.5$ GHz	-
Relative bandwidth f_r	1.14	-
Target range	-	0.8 cm
Target dimensions	-	27×20 cm

Figure 8 presents pictures and IR measurements of the target with different orientations. The blue lines show the acquired measurement data after background subtraction. On the left, in (a) and (c), the IR is dominated by a strong reflection originating from the surface of the plate. On the right, in (b) and (d), however, an extended echo is apparent dominated by the reflections of the two metal feet on the front.

To define the number of sinc functions for the model we assume that the pulse width is directly related to the physical dimensions of the target. Therefore, we select a model window covering a range of 27 cm corresponding to 1.8 ns of free space propagation. Given this, the number of sinc functions equals

$$N_s = \left\lceil \frac{N_f \cdot \Delta f}{\Delta S} \right\rceil = \lceil N_f \cdot \Delta f \cdot T_s \rceil = 8. \quad \text{(V.1)}$$

Furthermore, we select $N_e = 2$. Figures 8 (c) and (d) show the resulting model window and the estimated model. Since the model window covers the extended target echo and the estimated model shows a good agreement with the measurement data we conclude that $N_s = 8$ is a reasonable choice for this target. Hence, selecting N_s by the physical target dimensions is appropriate if no resonance effects occur at the target. Additionally, the pulse width indeed not only depends on the maximum physical dimension of the target but also on the orientation relative to the radar.

VI. Conclusion

In this paper we propose a multi-target signal model and a corresponding ML parameter estimator targeting UWB-radar applications. Our approach allows a joint estimation of global target parameters (range and velocity) as well as the characteristic dispersive signature of a target. We formulate the model and estimator as extensions to the RIMAX algorithm relaxing its model simplifications designed for narrower bandwidths.

The main impact of the high relative bandwidth is that typical model simplifications concerning the Doppler effect are not valid anymore. This has three major consequences. First, the Doppler effect results in a dispersive response in the Doppler spectrum requiring an explicit model for the relative target velocity instead of a Doppler shift-based approach. Second, the global target parameters range and velocity require coupling terms and cannot be estimated independent of each other, as performed by RIMAX. Third, the Doppler effect results in

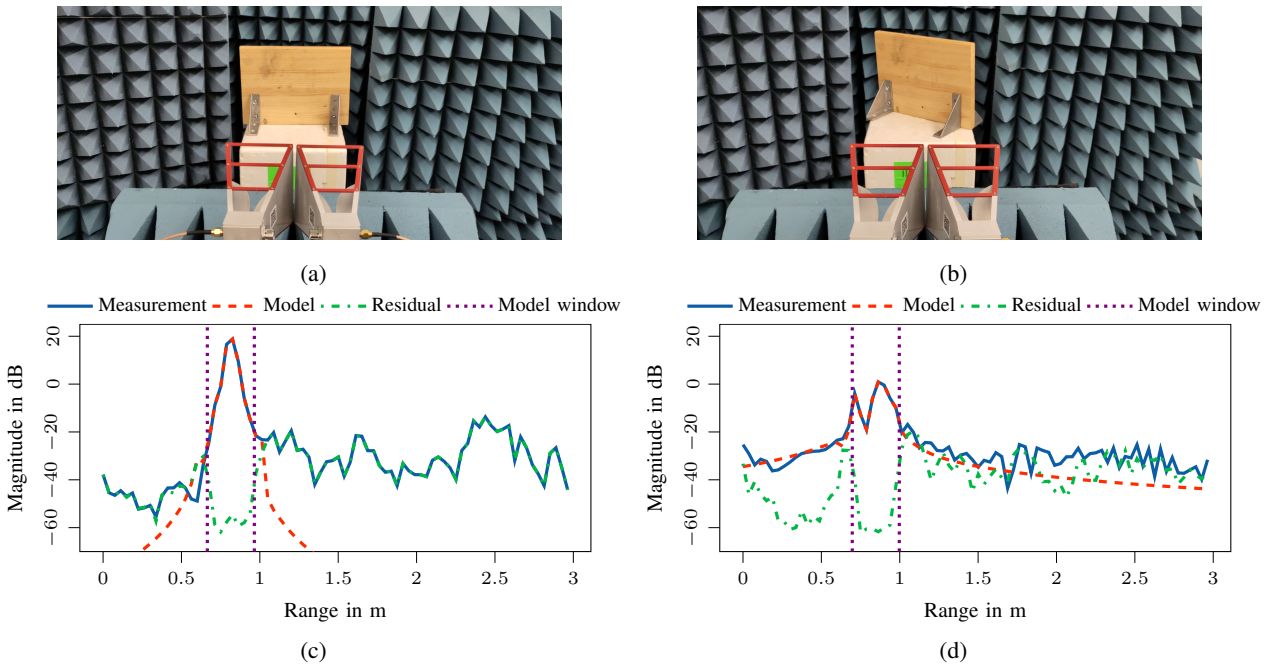

Fig. 8: Short range UWB radar measurements of an exemplary target with (a) and (b) showing pictures of the setup, and (c) and (d) showing corresponding IRs and estimated models.

a time-scaling of the extended target signature which needs to be considered during target response modeling. However, the aforementioned points are not equally important for all applications. While the velocity model and the parameter coupling is already necessary for small relative velocities, the Doppler scaling of the target response is only significant for high velocities. Therefore, we propose to compensate this scaling after the parameter estimation if required.

Regarding target response modeling we assume that the response is composed of contributions from individual closely spaced scattering centers. Instead of estimating these scattering points individually, we propose to use an FIR structure. This, however, requires a prior knowledge about the extent of the target response in fast time, i.e., the model order of the FIR structure. With this model, we can efficiently estimated extended target responses from noisy data. Nevertheless, this representation requires a clear separation of target responses in the considered parameter domains. Otherwise, the superposition of individual target responses is treated as belonging to a single target.

There are further extensions to the model worth analyzing. A model order selection based on statistical tests could render an assumption about the time extent of the target responses unnecessary. Furthermore, this would allow to use individual model orders for each target response. When it comes to resonant target structures, an extension by a recursive model is required. The estimator could be based on the Yule-Walker equations from autoregressive time series modeling. Additionally, an increase of the parameter space, e.g., by direction of arrival estimation, could improve the separation of individual target responses and would add further valuable global target parameters.

In this publication, we only considered a dispersive response in range. However, one could also imagine that a target is extended in other domains such as in velocity, e.g., caused by moving rotor blades of a drone. It is conceivable to expand the FIR approach also to this domain. Nevertheless, we expect a drawback in performance between the FIR approach applied to multiple domains and an estimation of point scatterers in the range-velocity domain and a subsequent clustering approach. This needs to be investigated.

Finally, the parametric representation of the target response allows a straightforward postprocessing of it. Hence, applications such as target recognition or imaging could be developed which directly incorporate the proposed model.

Appendix

1) Generalized Least-Squares: Considering (III.2) and (III.7) together with (III.6) and (II.9), we realize that the parameters $\boldsymbol{\gamma}$ play a different role than $\boldsymbol{\tau}$ and $\boldsymbol{\alpha}$.

Assume we are given estimates $\boldsymbol{\tau}^0$ and $\boldsymbol{\alpha}^0$ for delay and Doppler, respectively. The minimizers of

$$\min_{\tilde{\boldsymbol{\gamma}}} \left\| \mathbf{Y} - \tilde{\mathbf{S}}(\tilde{\boldsymbol{\gamma}}, \boldsymbol{\tau}^0, \boldsymbol{\alpha}^0) \right\|_F^2 \tag{A.1}$$

and respectively

$$\min_{\boldsymbol{\gamma}} \left\| \mathbf{Y} - \mathbf{S}(\boldsymbol{\gamma}, \boldsymbol{\tau}^0, \boldsymbol{\alpha}^0) \right\|_F^2 \tag{A.2}$$

are linear functions $\tilde{\boldsymbol{g}} : \mathbb{C}^{N_f \times N_t} \to \mathbb{C}^P$ and $\boldsymbol{g} : \mathbb{C}^{N_f \times N_t} \to \mathbb{C}^{P \times N_s + 2 \cdot N_e}$ with $\mathbf{Y} \mapsto \tilde{\boldsymbol{g}}(\mathbf{Y})$ and $\mathbf{Y} \mapsto \boldsymbol{g}(\mathbf{Y})$. Interestingly, in both cases they can be designed to constitute the Best Linear Unbiased Estimator (BLUE). If both the data $\mathbf{Y}$ and the parameter $\boldsymbol{\gamma}$ were vectors, the mapping $\boldsymbol{g}$ would be realized by the so called Moore-Penrose inverse. To avoid index-heavy notation, we skip the derivation of analytic expressions for $\tilde{\boldsymbol{g}}$ and $\boldsymbol{g}$ with the note that they can be derived analogously as the expressions of the Moore-Penrose matrices.

REFERENCES

[1] M. Vossiek, N. Haberberger, L. Krabbe, M. Hehn, C. Carlowitz, and M. Stelzig, "A tutorial on the sequential sampling impulse radar concept and selected applications," *IEEE Journal of Microwaves*, no. 1, 2023.

[2] J. Sachs, *Handbook of Ultra-Wideband Short-Range Sensing, Theory, Sensors, Applications*. Wiley-VCH Verlag GmbH & Co. KGaA, 2012.

[3] R. Thomä, R. H. Knöchel, J. Sachs, I. Willms, and T. Zwick, *Ultra-Wideband Radio Technologies for Communications, Localization and Sensor Applications*. InTech, 2013.

[4] R. Zetik, J. Sachs, and R. Thoma, "UWB short-range radar sensing - the architecture of a baseband, pseudo-noise UWB radar sensor," *IEEE Instrumentation & Measurement Magazine*, no. 2, 2007.

[5] S. Ley, S. Schilling, O. Fiser, J. Vrba, J. Sachs, and M. Helbig, "Ultra-wideband temperature dependent dielectric spectroscopy of porcine tissue and blood in the microwave frequency range," *Sensors*, no. 7, 2019.

[6] A. F. Molisch, "Ultra-wide-band propagation channels," *Proc. IEEE*, no. 2, 2009.

[7] S. Xu and A. Yarovoy, "Joint features extraction for multiple moving targets using (Ultra-)Wideband FMCW signals in the presence of Doppler ambiguity," *IEEE Trans. Signal Process.*, 2020.

[8] T. Dogaru, *Doppler processing with ultra-wideband (UWB) radar revisited -*. US Army Research Laboratory, 2018.

[9] M. Landmann, M. Kaske, and R. S. Thoma, "Impact of incomplete and inaccurate data models on high resolution parameter estimation in multidimensional channel sounding," *IEEE Trans. Antennas Propag.*, no. 2, 2012.

[10] M. Landmann, "Limitations of experimental channel characterisation," Ph.D. dissertation, Technische Universität Ilmenau, 2008.

[11] G. Matz, H. Bolcskei, and F. Hlawatsch, "Time-frequency foundations of communications: Concepts and tools," *IEEE Signal Processing Magazine*, no. 6, 2013.

[12] S. Kay and S. Doyle, "Rapid estimation of the range-doppler scattering function," *IEEE Transactions on Signal Processing*, no. 1, 2003.

[13] F. Hlawatsch and G. Matz, "Quadratic time-frequency analysis of linear time-varying systems," in *Wavelet Transforms and Time-Frequency Signal Analysis*, L. Debnath, Ed. Birkhäuser Boston, 2001.

[14] Y. He, P. Aubry, F. Le Chevalier, and A. Yarovoy, "Keystone transform based range-Doppler processing for human target in UWB radar," in *2014 IEEE Radar Conference*, IEEE, 2014.

[15] A. Ritcher, M. Landmann, and R. Thoma, "Maximum likelihood channel parameter estimation from multidimensional channel sounding measurements," in *The 57th IEEE Semiannual Vehicular Technology Conference, 2003. VTC 2003-Spring.*, IEEE, 2003.

[16] N. Iqbal, J. Luo, R. Muller, G. Steinbock, C. Schneider, D. A. Dupleich, S. Hafner, and R. S. Thoma, "Multipath cluster fading statistics and modeling in millimeter-wave radio channels," *IEEE Trans. Antennas Propag.*, no. 4, 2019.

[17] P. Swerling, "Probability of detection for fluctuating targets," *IRE Transactions on Information Theory*, no. 2, 1960.

[18] B. Chen, H. Liu, and Z. Bao, "Pca and kernel pca for radar high range resolution profiles recognition," in *IEEE International Radar Conference, 2005.*, 2005.

[19] K. Eom and R. Chellappa, "Noncooperative target classification using hierarchical modeling of high-range resolution radar signatures," *IEEE Transactions on Signal Processing*, no. 9, 1997.

[20] R. Zetik, H. Yan, E. Malz, S. Jovanoska, G. Shen, R. S., R. Salman, T. Schultze, R. Tobera, H.-I. Willms, L. Reichardt, M. Janson, T. Zwick, W. Wiesbeck, T. Deiler, and J. Thielecke, "Cooperative localization and object recognition in autonomous UWB sensor networks," in *Ultra-Wideband Radio Technologies for Communications, Localization and Sensor Applications*, R. Thomä, R. H. Knöchel, J. Sachs, I. Willms, and T. Zwick, Eds., InTech, 2013, ch. 9.

[21] S. Jovanoska, F. Govaers, and R. S. Thomä, *People tracking and data fusion for UWB radar applications*, 2017.

[22] R. Zetik, M. Eschrich, S. Jovanoska, and R. S. Thoma, "Looking behind a corner using multipath-exploiting UWB radar," *IEEE Trans. Aerosp. Electron. Syst.*, no. 3, 2015.

[23] S. Chang, M. Wolf, and J. W. Burdick, "An MHT algorithm for UWB radar-based multiple human target tracking," in *2009 IEEE International Conference on Ultra-Wideband*, IEEE, 2009.

[24] A. Richter, M. Landmann, and R. S. Thomä, "RIMAX - a flexible algorithm for channel parameter estimation from channel sounding measurements," in *COST 273 MCM*, ser. TD(04)045, 2004.

[25] S. Häfner, "Parameter estimation for broadband mm-wave FMCW MIMO radars - a model-based system identification perspectiv," Ph.D. dissertation, Technische Universität Ilmenau, 2021.

[26] M. Ershadh and M. Meenakshi, "A new modeling methodology for multipath parameter estimation in ultrawideband channels," *IEEE Trans. Antennas Propag.*, no. 4, 2021.

[27] K. Hausmair, K. Witrisal, P. Meissner, C. Steiner, and G. Kail, "SAGE algorithm for UWB channel parameter estimation," deutsch, in *COST 2100 Management Committee Meeting*, null ; Conference date: 03-02-2010 Through 05-02-2010, ., 2010.

[28] J. Salmi and A. F. Molisch, "Propagation parameter estimation, modeling and measurements for ultrawideband MIMO radar," *IEEE Trans. Antennas Propag.*, no. 11, 2011.

[29] G. Sun, C. Huang, Z. Cheng, R. He, B. Ai, and A. F. Molisch, "A study of clustering algorithms for time-varying multipath components in wireless channels," in *MILCOM 2021 - 2021 IEEE Military Communications Conference (MILCOM)*, IEEE, 2021.

[30] Z. Huang, R. Zhang, J. Pan, Y. Jiang, and D. Zhai, "A framework of multipath clustering based on space-transformed fuzzy c-means and data fusion for radio channel modeling," *IEEE Trans. Veh. Technol.*, no. 1, 2020.

[31] J. Gedschold, C. Schneider, M. Kaske, R. S. Thoma, G. Del Galdo, M. Boban, and J. Luo, "Tracking based multipath clustering in vehicle-to-infrastructure channels," in *2018 IEEE 29th Annual International Symposium on Personal, Indoor and Mobile Radio Communications (PIMRC)*, IEEE, 2018.

[32] C. Schneider, M. Ibraheam, S. Hafner, M. Kaske, M. Hein, and R. S. Thoma, "On the reliability of multipath cluster estimation in realistic channel data sets," in *The 8th European Conference on Antennas and Propagation (EuCAP 2014)*, IEEE, 2014.

[33] C. Kuang, C. Wang, B. Wen, and W. Huang, "An applied method for clustering extended targets with UHF radar," *#IEEE_O_ACC#*, 2020.

[34] C. Gentile, S. M. Lopez, and A. Kik, "A comprehensive spatial-temporal channel propagation model for the ultrawideband spectrum 2–8 GHz," *IEEE Trans. Antennas Propag.*, no. 6, 2010.

[35] R. Qiu, "A study of the ultra-wideband wireless propagation channel and optimum UWB receiver design," *IEEE J. Sel. Areas Commun.*, no. 9, 2002.

[36] L. Potter, D.-M. Chiang, R. Carriere, and M. Gerry, "A GTD-based parametric model for radar scattering," *IEEE Trans. Antennas Propag.*, no. 10, 1995.

[37] A. Moghaddar, Y. Ogawa, and E. Walton, "Estimating the time-delay and frequency decay parameter of scattering components using a modified MUSIC algorithm," *IEEE Trans. Antennas Propag.*, no. 10, 1994.

[38] A. Roussafi, N. Fortino, and J.-Y. Dauvignac, "UWB antenna 3D characterization using matrix pencil method," in *2014 IEEE Conference on Antenna Measurements & Applications (CAMA)*, IEEE, 2014.

[39] M. Khodjet-Kesba, K. E. K. Drissi, S. Lee, K. Kerroum, C. Faure, and C. Pasquier, "Comparison of matrix pencil extracted features in time domain and in frequency domain for radar target classification," *Int. J. Antenn. Propag.*, 2014.

[40] N. Shuley, "A review of uncooperative target identification using UWB resonance based radar techniques," *ECTI Transactions on Electrical Eng., Electronics, and Communications*, 2006.

[41] T. Sarkar and O. Pereira, "Using the matrix pencil method to estimate the parameters of a sum of complex exponentials," *IEEE Antennas Propag. Mag.*, no. 1, 1995.

[42] R. Saadane, A. M. Hayar, H. Hofstetter, and D. Aboutajdine, "Statistical UWB channel model parameters estimation based on SAGE algorithm," in *2007 Second International Conference on Communications and Networking in China*, IEEE, 2007.

[43] R. Carriere and R. Moses, "Autoregressive moving average modeling of radar target signatures," in *Proceedings of the 1988 IEEE National Radar Conference*, 1988.

[44] K. Haneda and J. Takada, "An application of SAGE algorithm for UWB propagation channel estimation," in *IEEE Conference on Ultra Wideband Systems and Technologies, 2003*, IEEE, 2003.

[45] B. Hanssens, E. Tanghe, D. P. Gaillot, M. Liénard, C. Oestges, D. Plets, L. Martens, and W. Joseph, "An extension of the RiMAX multipath estimation algorithm for ultra-wideband channel modeling," *EURASIP Journal on Wireless Communications and Networking*, no. 1, 2018.

[46] A. Richter Dr. - Ing., "Estimation of radio channel parameters," de, Ph.D. dissertation, Technische Universität Ilmenau, 2005.

[47] D. Cox and D. Hinkley, *Theoretical Statistics*, English, 1. ed., repr. Chapman and Hall/CRC, 1979, D. R. Cox; D. V. Hinkley, Literaturverz. S. 478 - 495.

[48] Y. Wang, J. Li, and P. Stoica, *Spectral Analysis of Signals, The Missing Data Case*. Springer International Publishing, 2005.
[49] J. Fessler and A. Hero, "Space-alternating generalized expectation-maximization algorithm," *IEEE Trans. Signal Process.*, no. 10, 1994.
[50] J. Martens, "New insights and perspectives on the natural gradient method," *J. Mach. Learn. Res.*, no. 146, 2020.

Jonas Gedschold received his M.Sc. degree in electrical engineering and information technology from Technische Universität Ilmenau, Germany, in 2018.

After working as Signal Processing Engineer at Emerson Automation Solutions from 2018 to 2020 in the area of gas analytics he joined the Electronic Measurement and Signal Processing Group at Technische Universität Ilmenau as research assistant and doctoral student. His research interests include signal processing and ultra-wideband radar applications with focus on nondestructive testing.

Sebastian Semper studied mathematics at Technische Universität Ilmenau, (TU Ilmenau), Ilmenau, Germany. He received the Master of Science degree in 2015. Since 2015, he has been a Research Assistant with the Electronic Measurements and Signal Processing Group, which is a joint research activity between the Fraunhofer Institute for Integrated Circuits IIS and TU Ilmenau, Ilmenau, In 2022 he finished his doctoral studies and received the doctoral degree with honors in electrical engineering. Since then, he has been a post doctoral student in the Electronic Measurements and Signal Processing Group. His research interest consist of compressive sensing, parameter estimation, optimization, numerical methods and algorithm design.

Michael Döbereiner received the B.Sc. and M.Sc. degrees in electrical engineering and information technology from the Technische Universität Ilmenau in 2017 and 2018.

He is currently working at the Fraunhofer Institute for Integrated Circuits IIS and a Dr.-Ing. candidate with research focus on high resolution parameter estimation in dynamic scenarios.

Reiner Thomä received his degrees in electrical engineering and information technology from TU Ilmenau, Germany. Since 1992, he has been a Professor at the same university. He has retired since 2018. In 2007, he received the Thuringian State Research Award for Applied Research and in 2014 the Vodafone Innovation Award, both for his contributions to high-resolution multidimensional channel sounding. In 2020, he received the EurAAP Propagation Award "For pioneering the multi-dimensional description of the mobile radio channel by advanced signal-processing methods." He has contributed to several European and German research projects and clusters. His research interests include multidimensional channel sounding, propagation measurement and model based parameter estimation, MIMO system over-the-air testing in virtual electromagnetic environments, MIMO radar, passive coherent location, and integrated communication and sensing.

Giovanni Del Galdo (M'12) received the Laurea degree in telecommunications engineering from the Politecnico di Milano, Milan, Italy, in 2002, and the Doctoral degree in MIMO channel modeling for mobile communications from Technische Universität Ilmenau (TU Ilmenau), Ilmenau, Germany, in 2007. He then joined the Fraunhofer Institute for Integrated Circuits, Erlangen, Germany, focusing on audio watermarking and parametric representations of spatial sound. Since 2012, he has been leading a joint research group composed of a Department at Fraunhofer Institute for Integrated Circuits IIS and, as a Full Professor, a Chair with TU Ilmenau on the research area of electronic measurements and signal processing. His current research interests include the analysis, modeling, and manipulation of multidimensional signals, over-the-air testing for terrestrial and satellite communication systems, and sparsity promoting reconstruction methods.